IEEE TRANSACTIONS ON POWER ELECTRONICS, VOL. 41, NO. 4, APRIL 2026 6811

Nonisolated Three-Switch DC–DC Converter Suppressing Leakage Currents in Low-Voltage DC Grid

Dongsu Lee, *Student Member, IEEE*, Juwon Lee, *Student Member, IEEE*, and Jung-Ik Ha, *Fellow, IEEE*

***Abstract*—Dc grids are recognized as a promising solution for next-generation power distribution systems due to their high efficiency and reduced energy conversion stages. Since modern electronic sources and loads operate with dc power, dc–dc converters serve as key components. In particular, nonisolated dc–dc converters are gaining attention due to their high efficiency and power density. However, the removal of galvanic isolation significantly lowers common-mode (CM) impedance, leading to increased leakage current and electric shock to users. To address these issues, a nonisolated three-switch converter topology is employed, which uses fewer switches while effectively suppressing CM currents. A low-frequency (LF) leakage current controller with a feedforward for enhanced transient response is developed, based on the CM equivalent circuit analysis. The operable range of the converter is analytically derived with consideration of the voltage fluctuations in both bipolar and unipolar dc grids. In addition, a hybrid pulsewidth modulation scheme is introduced to suppress high-frequency (HF) CM currents, along with the dc CMV injection method to enhance the suppression performance. Experimental results in the bipolar and unipolar grids confirm that the proposed methods effectively suppress both LF and HF CM currents, ensuring the user safety. The 11 kW hardware prototype achieves a peak efficiency of 99.38% and reduces the rms leakage current by over 91.35% compared to the conventional designs.**

***Index Terms*—Common mode voltage (CMV), dc–dc converter, leakage current, pulsewidth modulation (PWM), three-switch converter, transformerless converter.**

NOMENCLATURE

Superscript	*Low-frequency component of the variable*
CM	Common-mode.
CMV	Common-mode voltage.
DM	Differential-mode.
DMV	Differential-mode voltage.
HF	High-frequency.
LF	Low-frequency.
HB	Half-bridge.
FB	Full-bridge.
TS	Three-switch
EMI	Electromagnetic interference.
PE	Protective earth conductor.
U_k	kth active space vector of three-switch converter; $k \in \{1, \ldots, 8\}$.
M_k	Modulation method with center pivot U_k; $k \in \{1, 2, 3\}$.
T_{Uk}	Time interval of U_k; $k \in \{1, 2, 3\}$.
T_{sw}	Switching period.
S_x	Switch module; $x \in \{H, M, L\}$ denotes high-, mid-, and low-side.
g_x	Gating signal of switch; $x \in \{H, M, L\}$ denotes high-, mid-, and low-side.
v_p	Voltage at input positive terminal p.
v_n	Voltage at input negative terminal n.
v_q	Voltage at output positive terminal q.
v_r	Voltage at output negative terminal r.
v_{pn}	Voltage between input terminals p and n.
v_{qn}	Voltage between terminals q and n.
v_{rn}	Voltage between terminals r and n.
v_{qr}	Voltage between output terminals q and r.
v_{pm}	Voltage between terminals p and m.
v_{nm}	Voltage between terminals n and m.
v_{dm}	DM output voltage.
v_{cm}	Converter-generated CMV.
v_{dm}^*	Reference value of DMV of converter.
v_{cm}^*	Reference value of CMV of converter.
$v_{\mathrm{cm},g}$	Dc grid CMV.
$V_{\mathrm{cm},0}$	Supplementary dc CMV injected by converter.
V_{pn}	Nominal dc value of v_{pn}.
V_{qr}	Nominal dc value of v_{qr}.
i_{cm}	CM current.
d_{cm}	CM duty ratio.
d_{dm}	DM duty ratio.
R_N	Grounding resistance of utility grid.
R_G	Grounding resistance of local grid.
Z_H	Human body impedance.
L_{cm}	CM filter inductance.
L_{dm}	DM filter inductance.

Received 23 July 2025; revised 29 September 2025; accepted 20 October 2025. Date of publication 27 October 2025; date of current version 19 January 2026. This work was supported in party by the BK21 FOUR Program of the Education and Research Program for Future ICT Pioneers, Seoul National University, in part by the Seoul National University Electric Power Research Institute, in part by the National Research Foundation of Korea grant funded by the Korea Government (MSIT) under Grant RS-2024-00354687, and in part by Korea Institute of Marine Science and Technology Promotion funded by the Ministry of Oceans and Fisheries, Korea, under Grant RS-2023-00254688. Recommended for publication by Associate Editor M. Ordonez. *(Corresponding author: Jung-Ik Ha.)*

The authors are with the Department of Electrical and Computer Engineering, Seoul National University, Seoul 08826, South Korea (e-mail: babypighill0@snu.ac.kr; wronskian@snu.ac.kr; jungikha@snu.ac.kr).

Color versions of one or more figures in this article are available at https://doi.org/10.1109/TPEL.2025.3625952.

Digital Object Identifier 10.1109/TPEL.2025.3625952

C_{cm}	CM filter capacitance.
C_{dm}	DM filter capacitance.
C_y	Y-capacitance.
C_{dc}	Dc-link capacitance.

I. INTRODUCTION

DC GRIDS are a developing trend in future power distribution systems. They are compatible with renewable energy sources and distributed grids, which are in growing demand due to climate issues. In particular, low-voltage dc distribution systems are designed to be easily integrated for power supply in commercial or residential applications [1], [2], [3]. Most modern electronic sources and loads utilize dc, such as photovoltaic systems, power supplies in data centers, electric vehicle chargers, home appliances, lighting, and variable-frequency drives [1], [4]. Dc grids are regarded as a promising alternative to conventional ac systems due to their reduced power conversion stages and the absence of reactive power, resulting in improved efficiency [1], [5]. Despite these advantages, widespread adoption of the dc grid system has been inhibited due to unresolved concerns regarding grounding schemes, protection mechanisms, and system safety [2], [4], [5], [6], [7]. In response, the International Electrotechnical Commission has initiated standardization efforts for low-voltage dc systems [8], [9], and extensive research has been conducted on grounding and protection strategies in dc networks [4], [10], [11], [12], [13]. These grounding-related challenges are primarily associated with CM components, which induce circulating currents through unintended return paths.

Dc–dc converters play a key role as electrical interfaces between dc grids and dc loads. The electrical components involved in dc–dc converters consist of DM and CM components. DM components contribute to power transfer, while CM components flow through the ground or chassis, causing circulating currents that increase losses and raise concerns regarding both safety and EMI. To ensure electrical safety and block CM currents, conventional systems employ an isolated dc–dc converter with a high-frequency (HF) transformer [14], [15], as illustrated in Fig. 1(a). In Fig. 1(a), the current in line L is the DM component that delivers power. In contrast, the current in the PE conductor and the chassis is the CM component that does not contribute to power transfer and may instead raise grid-compatibility concerns. Because the transformer provides galvanic isolation, PE current is ideally zero. However, the adoption of transformers introduces additional energy conversion stages, which increase system complexity, cost, volume, and losses. To overcome these drawbacks, nonisolated converters, as shown in Fig. 1(b), have been developed to reduce the number of power conversion stages and lower losses [15], [16]. Despite their high efficiency, nonisolated converters encounter serious issues due to the absence of galvanic isolation, which creates a low-impedance CM path through the chassis. As a result, leakage current flows through the chassis as a CM path and returns either via the PE conductor to the grid or through the human body. Such current degrades grid compatibility when it flows through the PE conductor and poses an electric shock hazard when it flows through the human body. To address this challenge and ensure resilient and reliable power delivery in dc grid systems, especially when using nonisolated converters, further investigation into user protection and grid compatibility is essential.

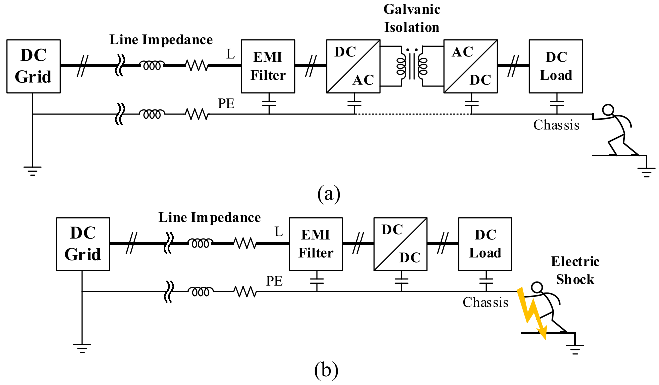

Fig. 1. DC–DC power conversion system configurations. (a) Isolated system employing a high-frequency transformer for galvanic isolation. (b) Nonisolated system.

To analyze the influence of CMV in this context, CMV sources are classified into two categories: HF CMV, produced by converter switching, and LF CMV, generated by the grid. These sources generate HF and LF CM currents, respectively. To mitigate HF CMV, various modulation techniques and converter topologies have been proposed. A bipolar modulation technique, typically implemented with a FB converter, is applied to reduce HF CM current by maintaining a constant CMV during each switching cycle [17], [18], [19]. The H5, H6, and HERIC topologies, as well as other ac–dc converter families, are designed to reduce HF CMV by decoupling the circuit in the zero DM voltage state [18], [19], [20], [21]. The same principle of maintaining a constant CMV is also applied in dc–dc converters, making these approaches effective in suppressing HF CM current. Additionally, filter-based techniques have been employed to mitigate HF CM current. Passive filters, such as third-order *LCL* floating filters, achieve compactness by using higher-order configurations to improve attenuation [22]. Active CM filters [23], [24] and hybrid filters [25] have also been proposed to enhance suppression performance further. However, these active filter approaches require additional components and power sources, such as magnetically coupled inductors operated by switching devices, auxiliary power supplies, and amplifiers. As another approach, common-ground converters are proposed, where both the input and output terminals share a common ground to achieve equipotential grounding and reduce CM current [26], [27], [28], [29], [30]. However, when the CM and DM conduction paths are shared within the converter, the magnitude of cross-coupling components significantly increases, resulting in elevated levels of CM noise. Although these strategies are effective in suppressing HF CM current, they are not suitable for suppressing LF CM currents induced by grid disturbances.

To effectively deal with LF CM currents, two types of approaches have been considered: circuit topologies that increase the LF CM impedance and control strategies that counteract LF CMV. One such approach is a high-frequency capacitive-coupled converter, which inserts a low-capacitance series capacitor into the resonant tank to raise a CM impedance at low frequencies [31], [32], [33]. However, operating at such high frequencies, often in the MHz range, degrades converter efficiency and limits the selection of available components. Therefore, a method of LF CM current mitigation via active LF CMV injection using differentially configured HB circuits, such as stacked HB or FB configurations, has been proposed. In previous studies, the stacked HB circuit is used to control CMV for input voltage balancing actively, rather than for LF CM current suppression [34], [35], [36]. In subsequent work, LF CMV is reduced by employing a stacked HB converter combined with a cascaded current source rectifier [37]. A related approach uses a FB converter to control LF CMV by actively injecting counteracting voltages to cancel grid-induced CMV [38], [39], [40]. However, this method is inadequate for addressing unexpected CMV sources such as system asymmetry or grid voltage fluctuations. To solve this problem, feedback-based approaches have been introduced to suppress LF CM current [41], [42]. However, all of these methods rely on dual-HB structures, inherently requiring at least four switches.

In this article, a nonisolated dc–dc converter topology with fewer switches is employed, and control and modulation methods are proposed to suppress leakage current. The rest of this article is organized as follows. Section II presents the CM equivalent circuit of a nonisolated converter in both bipolar and unipolar (monopolar) configurations and identifies the sources of LF CMV induced by the grid. Based on this analysis, a leakage current controller is implemented to reduce LF CM currents. Section III introduces a TS converter topology and evaluates its operating range that ensures effective mitigation performance under grid voltage fluctuations. In Section IV, a hybrid pulsewidth modulation (PWM) strategy is proposed to reduce HF CM current, along with a dc CMV injection method that enhances the HF CM current reduction. Section V validates the proposed control and modulation methods through simulation and experimental results based on a hardware prototype under voltage fluctuations in both bipolar and unipolar grids that simulate real grid situations. Finally, Section VI concludes this article. Furthermore, user safety is assessed by measuring touch currents in ground fault conditions.

II. COMMON-MODE ANALYSIS

This section describes grounding methods for low-voltage dc systems with nonisolated dc–dc converter systems. Based on the grounding method, the CM equivalent circuit of the entire system is derived. The transfer function of the CM current is analyzed in both low and high frequency ranges, emphasizing the necessity of active CMV control. Following this analysis, a leakage current controller is introduced, incorporating a feedforward CMV reference to improve transient response.

A. Configuration of System

The external conductor of the device, also known as the chassis, is designed to be physically accessible to the user. It is electrically connected to the ground of the grid through a PE cable. This configuration is closely associated with two primary concerns: 1) touch current and 2) leakage current. Touch current is defined as the current flowing through a user when they come into contact with the chassis. To ensure user safety, this current is limited to 3.5 mA [43]. Meanwhile, leakage current, which flows from the device to ground, has the potential to cause compatibility or power quality issues in the grid. To ensure the resilient operation of the system, leakage current is limited to 30 mA [9]. If this limit is exceeded, a residual current device (RCD), also known as a ground fault circuit interrupter, will disconnect the circuit from the system, leading to a power interruption. Therefore, to ensure user safety and enhance grid resilience by preventing nuisance tripping of the RCD, it is necessary to reduce both touch and leakage currents in the presence of unexpected CMV.

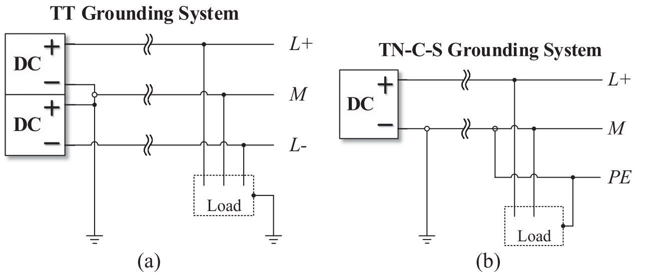

Fig. 2. Examples of DC grid polarity and grounding schemes. (a) Bipolar DC grid with TT grounding system. (b) Unipolar DC grid with TN-C-S grounding system.

In an isolated converter, the CM current is effectively blocked by the transformer, with a small portion flowing through the parasitic capacitance of device components, such as the transformer and heat sinks. In the nonisolated converter discussed in this study, the CM current is not blocked by the transformer. As a result, a low-impedance CM path is formed, which includes the filter, Y-capacitor, parasitic capacitances, and the enclosure ground [13]. Therefore, a comprehensive analysis of the enclosure grounding is essential to assess the leakage current flowing in nonisolated converters under both TT and TN methods [8]. In the TN method, as shown in Fig. 2(a), the device's chassis is connected to the neutral line (N); in the TT method, as shown in Fig. 2(b), the device's chassis is connected to a local ground [16]. The TN method bypasses most of the leakage current through the PE wire, due to its relatively low impedance compared to earth resistance. As a result, the touch current flowing through the human body is reduced, enhancing user safety. However, this configuration results in a higher total CM current through the converter. Moreover, if the PE line becomes disconnected, the entire CM current flows through the human body, significantly increasing the risk of electric shock. In this study, the TN grounding is used to represent the worst-case leakage current scenario, while grounding loss is considered to evaluate the worst-case touch current scenario.

In addition to the grounding configuration, the polarity of the dc grid also influences the CM current by altering the potential difference between the chassis and the ground. A dc grid adopts either a bipolar or unipolar structure. In a bipolar dc grid, positive

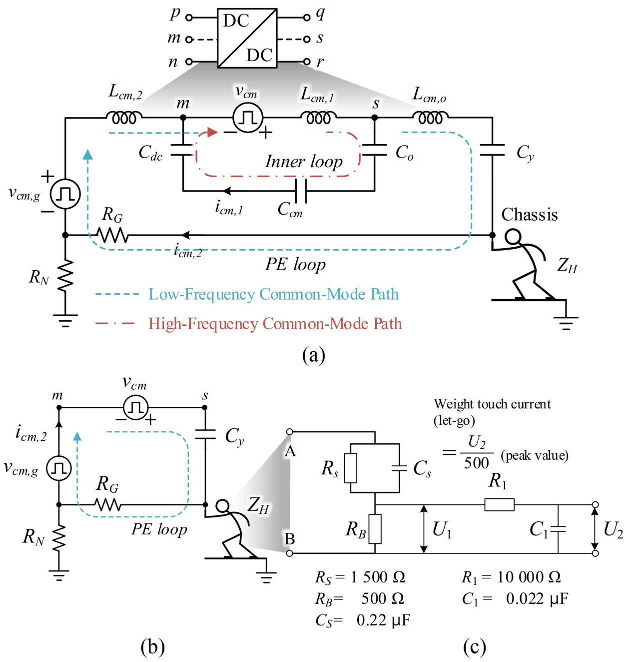

Fig. 3. CM equivalent circuit of a nonisolated DC–DC converter. (a) With floating filter. (b) Simplified representation in LF range. (c) Human body impedance model based on IEC 60990.

and negative dc voltages are supplied symmetrically with respect to the neutral line, as shown in Fig. 2(a). In a unipolar dc grid, only positive dc voltage is provided relative to the neutral line, as shown in Fig. 2(b). This study proposes leakage current reduction strategies that account for both grid configurations.

B. CM Equivalent Circuit Analysis

The converter is composed of three main components: 1) a third-order *LCL* filter to suppress HF EMI, 2) switching devices, and 3) Y-capacitors. HF CM EMI originates from the switching of the converter. The Y-capacitor, which is designed to mitigate sudden voltage spikes by bypassing HF CM current to ground, functions as a critical safety component in power electronic systems. It is positioned between the output terminal and the chassis, terminated at the midpoint of the output ports. However, while bypassing HF CM current, the Y-capacitance incidentally provides a path for LF leakage current. The exact value of the Y-capacitance is determined by the configuration and design of the converter's load side, which is often fixed by system-level constraints and reaches up to several thousand nF [44].

To define the CM equivalent circuit, it is first necessary to describe the CMV of both the converter and the grid. The CM component is defined as the average (sum) component of voltage or current. Consequently, the CM equivalent circuit is constructed by calculating the source and impedance between the virtual neutral points of the components [45], [46]. Let p and n represent the positive and negative poles of the input port, and let q and r represent the positive and negative poles of the output port, as illustrated in Fig. 3(a). Let m denote the virtual mid-point of the input, which corresponds to the average potential of the input ports $(p,\ n)$. Similarly, let s denote the virtual mid-point of the output, which corresponds to the average potential of the output ports (q, r). The CMV generated by the converter (v_{cm}) is defined as the voltage difference between the average potentials of output ports $(q,\ r)$ and the input ports $(p,\ n)$, and is expressed as

$$v_{\text{cm}} = \frac{v_q + v_r}{2} - \frac{v_p + v_n}{2}. \tag{1}$$

The CMV generated by the grid $(v_{\text{cm},g})$ is defined as the potential of m with respect to the ground. $v_{\text{cm},g}$ arises from several contributing factors, such as impedance imbalance [47], asymmetrical grid voltage [48], input and output voltage fluctuations [41], voltage drop across neutral line [49], external LF CMV [37], and power grid faults [50]. In the event of a grid line fault, the converter disconnects the circuit from the grid. Therefore, the leakage current suppression method is not applied in this scenario [51]. Under normal conditions, the CMV component caused by impedance imbalance (ΔZ) is expressed as

$$\overline{v_{\text{cm},g}} = \frac{\Delta Z}{\Sigma Z}\overline{v_{\text{dm}}} \tag{2}$$

where ΣZ is the sum of the impedances and v_{dm} is the DMV at the converter's output pole. The superscript bar $(\overline{\ })$ denotes the LF magnitude of the variable, indicating the mean value over one switching cycle. Fluctuations in input voltage result in the generation of an LF CMV between the input ports and the grid's neutral point. The resulting LF CMV depends on the grid polarity and is expressed as

$$\overline{v_{\text{cm},g}} = \frac{\overline{v_{pm}} + \overline{v_{nm}}}{2}\ \text{(bipolar)}$$
$$\overline{v_{\text{cm},g}} = \frac{\overline{v_{pn}}}{2}\ \text{(unipolar)}\,. \tag{3}$$

The CM equivalent circuit is shown in Fig. 3(a). It includes the EMI filter, the LF CMV source from the grid, and the CMV source generated by the converter. In this circuit, all LF CMV sources originating from the grid are modeled as $v_{\text{cm},g}$. R_G and R_N represent the equivalent series grounding resistances of the earth and utility grid, respectively. In TN grids, R_N is less than tens of ohms, and R_G is less than a few ohms [16]. Under a loss of grounding situation, R_G is considered to be open. Z_H is the human body impedance as outlined by IEC regulations for measuring the touch current, and the circuit in Fig. 3(c) is used for this purpose [52]. Using this circuit, the transfer function from the CMV source to the leakage current in the TN grounding system is expressed as

$$G_{\text{cm}}(s) = \frac{i_{\text{cm}}}{v_{\text{cm}}} = \frac{1}{Z_2 + Z_1 \parallel Z_3} \cdot \frac{Z_1}{Z_1 + Z_3}$$
$$\text{where } Z_1 = \frac{1}{s2C_{\text{dc}}} + \frac{1}{sC_{\text{cm}}} + \frac{1}{s2C_{\text{dm},1}}$$
$$Z_2 = sL_{\text{cm},1} + (sL_{\text{dm},1}/2)$$
$$Z_3 = sL_{\text{cm},o} + (sL_{\text{dm},2}/2) + \frac{1}{s2C_Y} + R_G + sL_{\text{cm},2}. \tag{4}$$

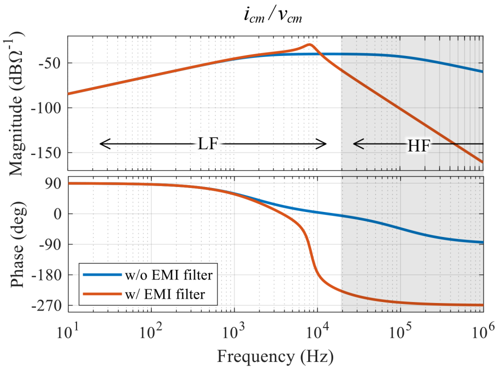

Fig. 4. Bode plot of the transfer function from the CMV source to the leakage current flowing through the PE conductor.

The Bode diagram of the transfer function, with and without an EMI filter, is shown in Fig. 4. HF CMVs above the switching frequency are mitigated by EMI filters, while slow transient CMVs below a few hertz are blocked by Y-capacitance. However, as shown in Fig. 4, LF CMV components within the frequency range above several tens of hertz and below the switching frequency remain unattenuated by both the Y-capacitor and EMI filter. To address this issue, active CMV control, implemented by injecting LF CMV through the converter, is employed to suppress leakage current in the LF range effectively. When combined with an EMI filter, this approach contributes to the overall reduction of leakage current across both LF and HF ranges. To further simplify the CM equivalent circuit for controller design, the frequency characteristics of the passive elements are considered. In the frequency region below the cutoff frequency of the *LCL* EMI filter, the series inductor exhibits negligible impedance, while the parallel capacitor exhibits very high impedance. Under these conditions, the original CM equivalent circuit in Fig. 3(a) reduces to the simplified model in Fig. 3(b). The LF CMV of the converter is represented between the virtual neutral points m and s. This simplified circuit is used to design the CM leakage current controller.

C. Controller Design

The block diagram of the leakage current controller, which actively controls the LF CMV to suppress leakage current, is illustrated in Fig. 5. The DM and CM currents are decoupled, enabling independent control of power transfer and leakage current. Using feedback from the current sensors, the DM and CM currents are regulated by the PI and PII controllers, respectively. The output of each controller serves as the reference for DMV and CMV, and the controller gain values are selected based on [41]. The leakage current controller provides feedback control for the CM current, thereby reducing the uncompensated CMV induced by grid disturbances. To improve the transient response of the leakage current controller, feedforward references are proposed. The simplified equivalent circuit of Fig. 3(a) in the LF range is shown in Fig. 3(b). To suppress LF CM current, the converter is controlled to maintain a constant potential difference across the Y-capacitors. Accordingly, the feedforward reference utilizes (3), which describes the LF CMV induced by grid polarity. Consequently, the final feedforward references, which compensate for grid voltage disturbances, are defined for both bipolar and unipolar grids as follows:

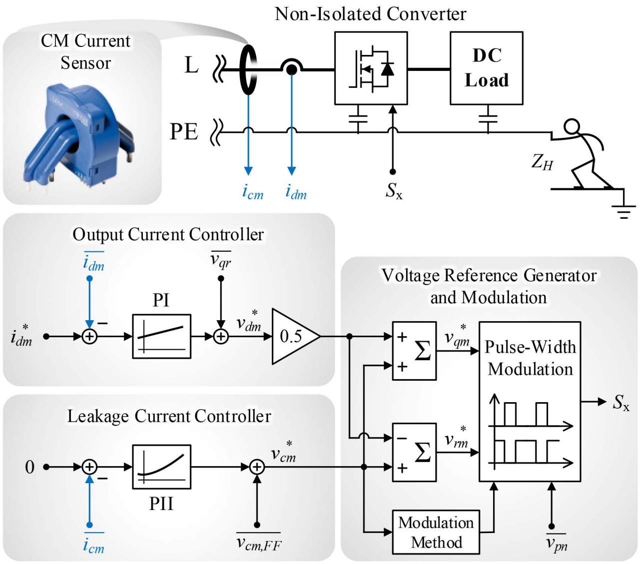

Fig. 5. Block diagram of the nonisolated converter controller capable of independently controlling CM and DM current.

$$v^*_{\mathrm{cm},FF} = V_{\mathrm{cm},0} - \left(\overline{v_{\mathrm{cm},g}} + \frac{\overline{v_{pm}} + \overline{v_{nm}}}{2}\right) (\text{bipolar})$$

$$v^*_{\mathrm{cm},FF} = V_{\mathrm{cm},0} - \left(\overline{v_{\mathrm{cm},g}} + \frac{\overline{v_{pn}} - V_{pn}}{2}\right) (\text{unipolar}). \quad (5)$$

V_{pn} is defined as the nominal constant value of v_{pn}. $V_{\mathrm{cm},0}$ denotes the supplementary dc CMV injected by the converter, whose characteristics are analyzed in detail in Sections III and IV. Given the infinite CM impedance of the converter at 0 Hz due to the Y-capacitor, the dc CMV does not affect the steady-state leakage current. In designing the leakage current controller, it should be noted that the cutoff frequency of the EMI filter constrains the achievable bandwidth. As the controller gain increases, the closed-loop bandwidth approaches this cutoff frequency, where the simplified CM equivalent circuit is no longer valid, leading to a tradeoff between controller performance and modeling accuracy.

III. TS CONVERTER TOPOLOGY

In this section, a comparative analysis of conventional HB, FB, stacked HB, and TS converters is performed. Furthermore, the TS converter is employed as the optimal topology for leakage current suppression. The operating range analysis of the converter is performed to ensure the performance of the leakage current suppression controller under voltage fluctuations that occur in real dc systems.

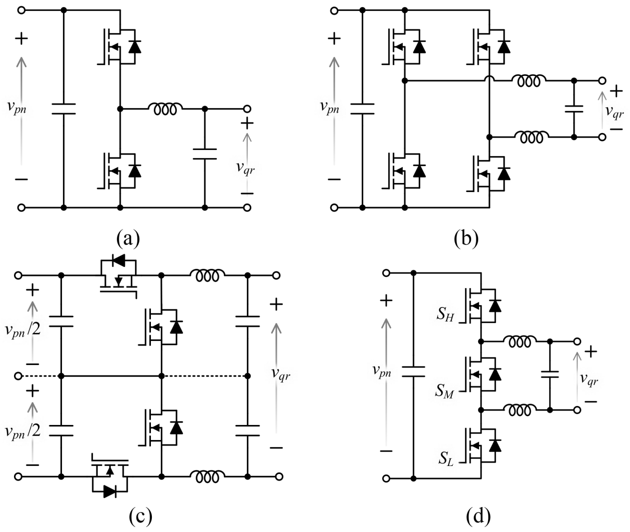

(a) (b) (c) (d)

Fig. 6. Comparison of converter topologies based on HB structures. (a) Conventional HB converter. (b) Full-bridge (FB) converter. (c) Stacked HB converter (dashed lines are optional depending on the number of output ports). (d) TS converter.

A. Half-Bridge Based Nonisolated Converter Topology

Single-leg HB converters, as depicted in Fig. 6(a), and their common grounded dc–dc converter families [26], [27], [28], [29], [30] are effective solutions employed in nonisolated dc–dc converters. They have the advantages of using fewer switches and passive elements, relatively simple configuration, and achieving high efficiency [26], [27], [29]. However, the common-ground converter exhibits a limitation: the LF DMV and CMV are dependent on each other because the ground of the input and output is connected, which fails to suppress LF CM current under grid voltage fluctuations. To address this limitation, configuring the output ports of two distinct HB converters differentially is a viable solution, as illustrated in Fig. 6(b), (c), and (d).

The FB converter topology, as shown in Fig. 6(b), configures the output poles of two parallel-connected HBs differentially. Research has been conducted to suppress leakage current by generating LF CMV [38], [39], [40], [41]. However, the FB converter has the limitation of using twice as many switches and inductors as the conventional HB converter, which increases cost and causes higher switch-related losses. The FB converter uses a total of four switches. The average number of conducting switches per switching cycle is two, and it requires at least four switching events in each cycle to generate LF CMV. By contrast, the HB converter requires only two switches, with one conducting on average and two switching events per cycle.

The stacked HB converter topology, as illustrated in Fig. 6(c), configures the output poles of two series-connected HBs differentially. Research has been conducted to suppress leakage current by generating LF CMV [37], [42]. Compared to the FB converter, the stacked HB converter reduces the voltage stress on each switch, enabling the use of lower-rated devices. The stacked HB converter uses a total of four switches. The average number of conducting switches per switching cycle is two, and it requires at least four switching events per cycle to generate LF CMV. However, it requires two input capacitors and a neutral current in bipolar grids to balance input voltages during CMV injection, which increases system complexity and grid losses [5]. Moreover, when connected to a unipolar grid, simultaneous CMV control and input capacitor voltage balancing are incompatible, resulting in a voltage imbalance of the input capacitor. In addition, the magnitude of the maximum injected CMV is limited to approximately half of that achievable with the FB and the TS converter [34], [35], [36].

TABLE I
COMPARISON OF CONVERTER TOPOLOGIES

	LF CMV Control	***Total # Switches***	***Avg. # conducting switches***	***Avg. # switching events***
HB Conv. [30]	Unavailable	2	1	2
FB Conv. [38], [39], [40], [41]	Available	4	2	4
Stacked HB Conv. [37], [42]	Available	4	2	4
TS Conv. [52], [53]	Available	3	$1+D(\leq 2)$	3 or 4

The TS converter is derived by integrating two intermediate-side switches in a stacked HB converter. This topology has been previously adopted in multiport converters [53], [54], [55] and in three-phase configurations for dual-motor drives [56], but these implementations neither use a single-output configuration nor address LF CMV mitigation. In this article, the TS converter is implemented as a single-input–single-output structure for generating CMV. By configuring the output poles differentially, it enables active LF CMV control similar to the FB and stacked HB converters. By reducing the number of switches to three, the topology lowers both system cost and switch-related losses. The number of switches conducting during a switching cycle is either 1 or 2, with an average $1+D$, where D is the DM duty ratio ranging from 0 to 1. Therefore, the conduction loss of the switch is reduced compared to the FB converter. The number of switching events per switching cycle is typically three or four, depending on the modulation schemes. The switching loss analysis with respect to the number of switches is discussed in detail in Section IV. Unlike stacked HB converters, the TS converter does not require neutral current in the input capacitor to control CMV. As a result, the TS converter enables precise CMV control without relying on neutral current, even in unipolar grid configurations. The characteristics of the converters are summarized in Table I.

In summary, the TS converter exhibits the limitation of requiring an additional switch and higher losses than the conventional HB, which is unable to inject LF CMVs. However, in comparison to FB, which can inject LF CMVs, this topology has the advantage of requiring fewer switches and lower losses while maintaining equivalent LF CMV injection performance. Furthermore, in contrast to the stacked HB converter, this design

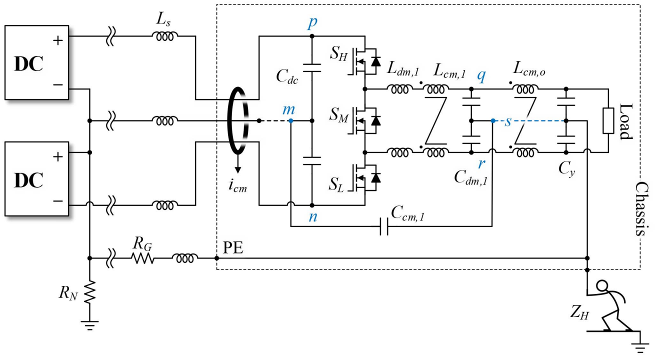

Fig. 7. Power circuit diagram of the nonisolated TS DC–DC converter for suppressing leakage current. A bipolar DC grid with a TN grounding system is assumed (dashed lines are optional, depending on the configuration of the input ports).

does not require a neutral point current and does not result in input voltage unbalancing. A comparative analysis of CM current suppression between topologies is presented through simulation in Section V. The power circuit, EMI filter, and Y-capacitor of the TS converter connected to a bipolar grid are shown in Fig. 7.

B. Operating Range Analysis

The output voltages of the TS converters are inherently bounded by the input voltage. As the LF CMV injection introduces a uniform voltage bias to the output poles, its allowable range is likewise influenced by both input and output voltages. In this context, the allowable LF CMV range and the input–output voltage ratio are mutually dependent. For example, under high voltage-gain operation, such as when the input–output voltage ratio d_{dm} of the converter is close to 0 or 1, the allowable CMV range is strongly affected: when d_{dm} is close to 0, the reduced DMV provides a larger margin for CMV injection, whereas when d_{dm} is close to 1, the increased DMV narrows the available CMV range. Therefore, analyzing the valid operating region is essential to ensure reliable suppression of LF CM current under grid disturbances. The DM duty ratio, which is the normalized DMV of the converter, is denoted by d_{dm}. The CM duty ratio, which is the normalized CMV of the converter, is d_{cm}. Both are defined by

$$d_{\mathrm{dm}} = v_{\mathrm{dm}}^{*}/\overline{v_{pn}}, d_{\mathrm{cm}} = v_{\mathrm{cm}}^{*}/\overline{v_{pn}}. \tag{6}$$

Given that the effect of the inductance is negligible in the LF range, the potential at the output port and the potential at the bridge pole are regarded as equal. Consequently, the range of output voltages, denoted as $\overline{v_{qn}}$ and $\overline{v_{rn}}$, is limited by the input voltage $\overline{v_{pn}}$. Furthermore, due to the inherent characteristics of the TS converter, $\overline{v_{qn}}$ is invariably greater than $\overline{v_{rn}}$. This relationship is expressed using the following equation:

$$\begin{cases} 0 \le \overline{v_{qn}} \le \overline{v_{pn}} \\ 0 \le \overline{v_{rn}} \le \overline{v_{pn}} \\ \overline{v_{qn}} \ge \overline{v_{rn}} \end{cases}, \begin{cases} d_{\mathrm{dm}} + 2d_{\mathrm{cm}} \le 1 \\ -d_{\mathrm{dm}} + 2d_{\mathrm{cm}} \ge -1 \\ d_{\mathrm{dm}} \ge 0. \end{cases} \tag{7}$$

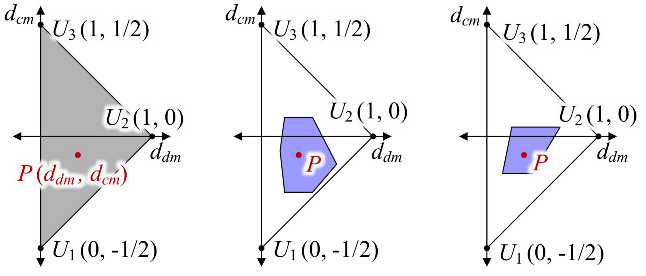

(a) (b) (c)

Fig. 8. Operating point traces under voltage fluctuation. (a) Entire operable range. (b) Operating range in a bipolar grid with ±20% input/output voltage fluctuation around a nominal voltage ratio of 0.5. (c) Same condition in a unipolar grid.

The relationship expressed in (7) defines a triangular region in the two-dimensional vector space formed by the duty ratios d_{dm} and d_{cm}, as shown in Fig. 8(a). The operating point P is required to lie within this triangular region.

In a bipolar grid, the duty ratios to synthesize CMV and DMV references are approximated as

$$\begin{aligned} d_{\mathrm{dm}} &\approx \frac{\overline{v_{qr}}}{\overline{v_{pn}}} \\ d_{\mathrm{cm}} &\approx \frac{V_{\mathrm{cm},0} - \left(\overline{v_{\mathrm{cm},g}} + \frac{\overline{v_{pm}}+\overline{v_{nm}}}{2}\right)}{\overline{v_{pn}}}. \end{aligned} \tag{8}$$

Assuming ideal tracking of the DM and CM voltage references by the converter, the operating point P traces a hexagonal region in Fig. 8(b), ensuring effective suppression of LF CM currents under grid-induced disturbances. The additionally injected dc CMV component $V_{\mathrm{cm},0}$ shifts the hexagonal operating region along the d_{cm} axis. To ensure proper LF CM current suppression, the shifted hexagon remains within the outer triangular boundary defined by (7). This shift does not affect the steady-state leakage current, since dc CMV components do not generate leakage current through the Y-capacitor. Accordingly, $V_{\mathrm{cm},0}$ serves as an additional degree of freedom, whose allowable range is bounded as follows:

$$\begin{aligned} \max\left(\overline{v_{\mathrm{cm},g}} + \frac{1}{2}\overline{v_{qr}} + \overline{v_{nm}}\right) &\le V_{\mathrm{cm},0} \\ &\le \min\left(\overline{v_{\mathrm{cm},g}} - \frac{1}{2}\overline{v_{qr}} + \overline{v_{pm}}\right). \end{aligned} \tag{9}$$

When $V_{\mathrm{cm},0}$ lies within the voltage range defined in (9), the converter effectively mitigates LF CM current while maintaining proper DMV control performance. For instance, with ±10% variation in both input and output voltages in a bipolar grid, the lower and upper bounds of $V_{\mathrm{cm},0}$ as a function of voltage ratio are shown in Fig. 9(a), based on the limits defined in (9). At a voltage ratio of 0.7, the corresponding $V_{\mathrm{cm},0}$ is limited to the range $[-0.065\ V_{pn}, 0.065\ V_{pn}]$. The maximum achievable voltage ratio is constrained to 0.818, corresponding to the intersection point of the two boundaries illustrated in Fig. 9(a). When the converter addresses not only input/output voltage fluctuations but also grid CMV, the allowable range for LF CM suppression

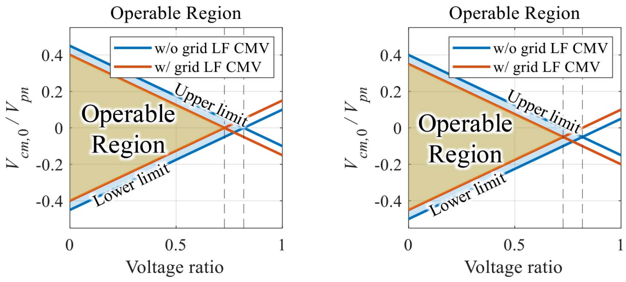

(a) (b)

Fig. 9. Range of additionally injectable DC CMV at a nominal voltage ratio of 0.7, considering ±10% variation in input/output voltages and ±5% variation in grid LF CMV with respect to the nominal input voltage. (a) Bipolar grid. (b) Unipolar grid.

is further reduced. For instance, when the grid CMV is bounded within ±0.05 V_{pn}, the allowable range of $V_{\mathrm{cm},0}$ is reduced to $[-0.15\,V_{pn}, 0.15\,V_{pn}]$, and the maximum voltage ratio becomes limited to 0.727.

In a unipolar grid, the duty ratios are approximated as

$$d_{dm} \approx \frac{\overline{v_{qr}}}{\overline{v_{pn}}}$$

$$d_{\mathbf{cm}} \approx \frac{V_{\mathrm{cm},0} - \left(\overline{v_{\mathrm{cm},g}} + \frac{\overline{v_{pn}} - V_{pn}}{2}\right)}{\overline{v_{pn}}}. \tag{10}$$

Assuming the same consumption as that of the bipolar case, the operating point P traces a trapezoidal region in Fig. 8(c), ensuring effective suppression of LF CM currents under grid-induced disturbances. $V_{\mathrm{cm},0}$ also shifts the trapezoidal operating region along the d_{cm} axis, as long as it remains within the outer triangular boundary defined by (7). The allowable range of $V_{\mathrm{cm},0}$ is bounded as follows:

$$\max\left(\overline{v_{\mathrm{cm},g}} + \frac{1}{2}\overline{v_{qr}} - \frac{1}{2}V_{pn}\right) \leq V_{\mathrm{cm},0}$$

$$\leq \min\left(\overline{v_{\mathrm{cm},g}} - \frac{1}{2}\overline{v_{qr}} - \frac{1}{2}V_{pn} + \overline{v_{pn}}\right). \tag{11}$$

For instance, with ±10% variation in both input and output voltages in a unipolar grid, the lower and upper bounds of $V_{\mathrm{cm},0}$ as a function of voltage ratio are shown in Fig. 9(b), based on the limits defined in (11). At a voltage ratio of 0.7, the corresponding $V_{\mathrm{cm},0}$ is limited to the range $[-0.115\,V_{pn}, 0.015\,V_{pn}]$. The maximum achievable voltage ratio is constrained to 0.818, corresponding to the intersection point of the two boundaries illustrated in Fig. 9(b). To cope with a grid CMV bounded within ±0.05 V_{pn}, the allowable range of $V_{\mathrm{cm},0}$ is reduced to $[-0.065\,V_{pn},\ 0.035\,V_{pn}]$, and the maximum voltage ratio becomes limited to 0.727.

IV. PROPOSED PWM

This section presents a carrier-based PWM for the TS converter, which generates both DMV and CMV references. The effective active vector states are identified, and their corresponding time intervals are derived. Based on these vectors, various modulation schemes are proposed and analyzed with respect to their impact on HF leakage current. A hybrid modulation technique is introduced to suppress HF leakage current, and a dc CMV injection method is proposed to improve leakage current reduction. In addition, the switching loss characteristics of the proposed modulation method are analyzed.

TABLE II
ACTIVE STATES OF THE TS CONVERTER

	$\boldsymbol{U_1}$	$\boldsymbol{U_2}$	$\boldsymbol{U_3}$	$\boldsymbol{U_4}$	$\boldsymbol{U_5}$	$\boldsymbol{U_6}$	$\boldsymbol{U_7}$	$\boldsymbol{U_8}$
$\boldsymbol{g_H}$	0	1	1	0	0	1	1	0
$\boldsymbol{g_M}$	1	0	1	0	1	0	1	0
$\boldsymbol{g_L}$	1	1	0	1	0	0	1	0

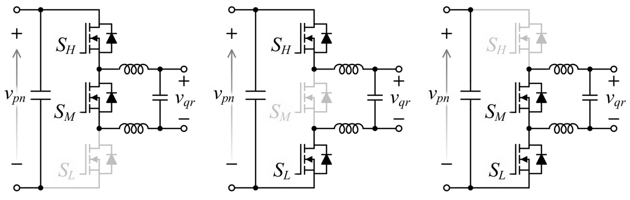

(a) (b) (c)

Fig. 10. Equivalent circuit diagrams of the three basic active switching states. (a) $\boldsymbol{U}_1$. (b) $\boldsymbol{U}_2$. (c) $\boldsymbol{U}_3$.

TABLE III
DMV AND CMV VALUES OF THREE ACTIVE STATES

	$\boldsymbol{U_1}$	$\boldsymbol{U_2}$	$\boldsymbol{U_3}$
v_{dm}	0	v_{pn}	0
v_{cm}	$-v_{pn}/2$	0	$v_{pn}/2$

A. PWM for TS Converter

The converter has eight possible switching states, denoted from U_1 to U_8, as listed in Table II. The high-, mid-, and low-side switches are denoted by S_H, S_M, and S_L, while their corresponding gating signals are represented by g_H, g_M, and g_L, respectively. Among the switching states, U_7 is excluded due to the risk of a shoot-through fault that directly shorts the input source. U_4, U_6, and U_8 are also avoided because they enable mid-side diode conduction during switching transitions, which degrades efficiency and DMV regulation. U_5 reduces switching losses by decreasing the number of switching transitions, but it results in both high- and low-side switches being in diode conduction. As a result, the CMV becomes passively dependent on the instantaneous direction of the CM current, which limits the injection of LF CMV. One way to address this issue is to employ bidirectional switches that block CM current. However, such configurations are beyond the scope of this study. Based on these considerations, U_1, U_2, and U_3 are selected as the active vector states. The circuit modes in each active vector are illustrated in Fig. 10(a), (b), and (c), which correspond to U_1, U_2, and U_3, respectively. In each state, the instantaneous DMV and CMV applied by the converter are summarized in Table III. The duration times T_{U1}, T_{U2}, and T_{U3} within a single switching

TABLE IV
COMPARE VALUES AND SWITCHING EVENTS BY MODULATION STRATEGY

Modulation type (Center pivot)	**High compare value ($\mathrm{CMP_H}$)**	**Low compare value ($\mathrm{CMP_L}$)**	**Switching event of S_H when down-carrier meets CMP**	**Switching event of S_M when down-carrier meets CMP**	**Switching event of S_L when down-carrier meets CMP**
M_1 (U_1)	$(T_{U1}+T_{U3})/T_{sw}$	T_{U3}/T_{sw}	Reset at $\mathrm{CMP_L}$ Set at $\mathrm{CMP_H}$	Reset at $\mathrm{CMP_H}$	Set at $\mathrm{CMP_L}$
M_2 (U_2)	$(T_{U2}+T_{U3})/T_{sw}$	T_{U3}/T_{sw}	Reset at $\mathrm{CMP_H}$	Reset at $\mathrm{CMP_L}$ Set at $\mathrm{CMP_H}$	Set at $\mathrm{CMP_L}$
M_3 (U_3)	$(T_{U1}+T_{U3})/T_{sw}$	T_{U1}/T_{sw}	Set at $\mathrm{CMP_L}$	Reset at $\mathrm{CMP_H}$	Reset at $\mathrm{CMP_L}$ Set at $\mathrm{CMP_H}$

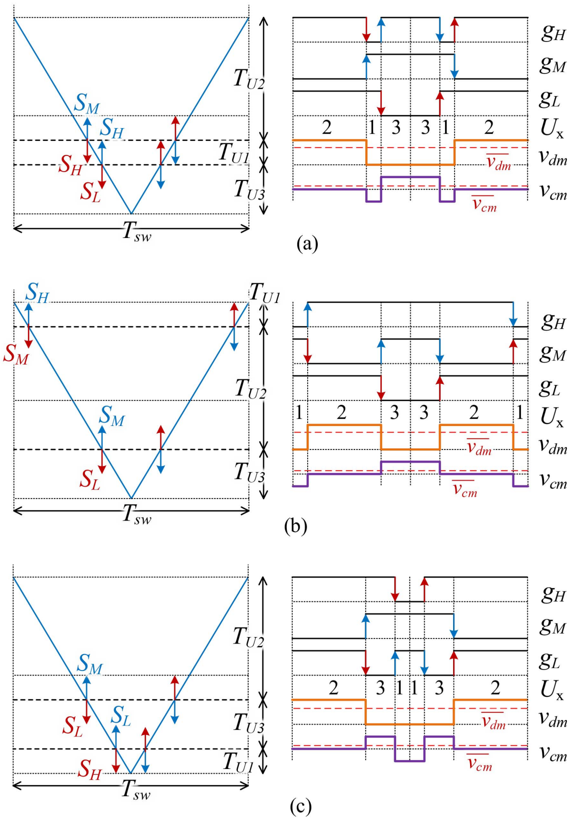

Fig. 11. Switching patterns using a symmetrical down-up carrier. (a) $\boldsymbol{M}_1$ with center pivot $\boldsymbol{U}_1$. (b) $\boldsymbol{M}_2$ with center pivot $\boldsymbol{U}_2$. (c) $\boldsymbol{M}_3$ with center pivot $\boldsymbol{U}_3$.

cycle are expressed using the converter's duty ratio d_{dm}, d_{cm}, and the switching period T_{sw}, as shown in

$$\begin{aligned} T_{U1} &= \frac{1-d_{\mathrm{dm}}-2d_{\mathrm{cm}}}{2} \cdot T_{sw} \\ T_{U2} &= d_{\mathrm{dm}} \cdot T_{sw} \\ T_{U3} &= \frac{1-d_{\mathrm{dm}}+2d_{\mathrm{cm}}}{2} \cdot T_{sw}. \end{aligned} \tag{12}$$

In order to enhance the precision of current sensing and to eliminate the subharmonic components of CMV, a symmetrical carrier-based PWM is employed. Three modulation methods are defined based on the selection of the center pivot vector. Specifically, modulation sequences centered at U_1, U_2, and U_3 are referred to as M_1, M_2, and M_3, respectively. The modulation is implemented using a down-up carrier and two compare values, as shown in Fig. 11. The required compare values and the corresponding set/reset switching actions for each modulation sequence are summarized in Table IV. When the up-carrier encounters the compare values, the set and reset signals for the switch are triggered in the opposite order.

B. High-Frequency Common-Mode Current Suppression

Depending on the modulation method described in Table IV, the CMV waveform exhibits distinct waveforms, as illustrated by the purple waveform in Fig. 11. The rms leakage current for each modulation method (M_1–M_3) is calculated by first deriving the CMV harmonic components using

$$\begin{aligned} v_{\mathrm{cm}}\ (n) &= \frac{2v_{pn}}{\pi n}\begin{Bmatrix} 2\sin\left(n\pi T_{U3}\right) \\ -\sin\left(n\pi\left(T_{U1}+T_{U3}\right)\right)\end{Bmatrix}(M_1) \\ v_{\mathrm{cm}}\ (n) &= \frac{2v_{pn}}{\pi n}\begin{Bmatrix} \sin\left(n\pi T_{U1}\right) \\ +\sin\left(n\pi T_{U3}\right)\end{Bmatrix}(M_2) \\ v_{\mathrm{cm}}\ (n) &= \frac{2v_{pn}}{\pi n}\begin{Bmatrix} \sin\left(n\pi\left(T_{U1}+T_{U3}\right)\right) \\ -2\sin\left(n\pi T_{U1}\right)\end{Bmatrix}(M_3) \end{aligned} \tag{13}$$

and then applying the system transfer function defined in (4). The rms value of the attenuated leakage current is calculated using the transfer function of the system, as outlined in (4). The resultant rms value is plotted over the duty ratio domain, as illustrated in Fig. 12. The leakage current using M2 in Fig. 12(b) exhibits the most significant leakage current. Meanwhile, M_1 achieves the minimum leakage current when the CMV reference is negative, whereas M_3 shows the lowest leakage current when the CMV reference is positive. Based on this observation, a hybrid modulation strategy is proposed, in which M_1 and M_3 are selectively applied depending on the sign of the CMV reference to reduce HF leakage current over the entire operation range, as shown in Fig. 12(d).

The trajectory of the minimum leakage current, shown as a red dashed line in Fig. 12(d), represents the condition where the leakage current is minimized. The EMI filter plays a decisive role in determining the HF CM current magnitude, particularly in response to harmonic variations introduced by different modulation methods. Consequently, minimizing the fundamental component of the CMV becomes the most effective strategy for reducing HF leakage current. Accordingly, the minimum-current trajectory approximately aligns with the condition where the fundamental component of CMV becomes zero, expressed

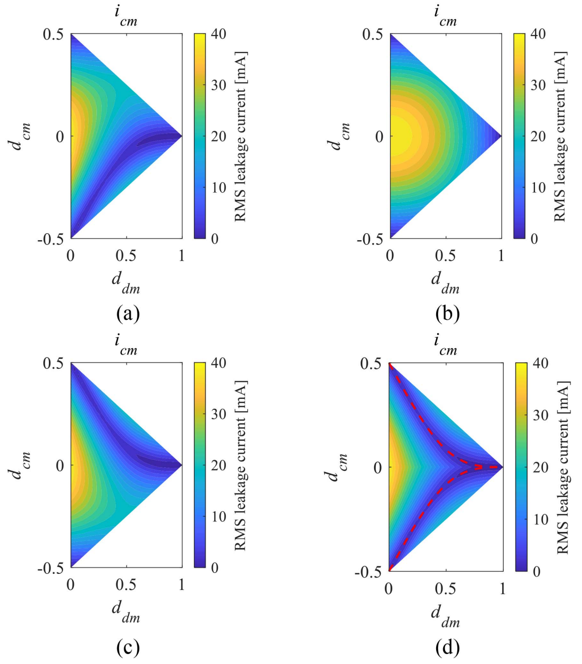

(a) (b)

(c) (d)

Fig. 12. Rms leakage current of the TS converter with different modulation schemes. (a) $\boldsymbol{M}_1$. (b) $\boldsymbol{M}_2$. (c) $\boldsymbol{M}_3$. (d) Hybrid modulation.

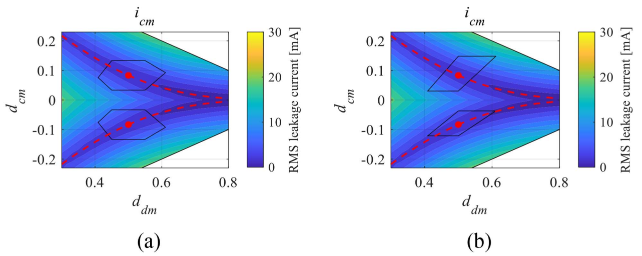

(a) (b)

Fig. 13. Operable region of the TS converter using hybrid modulation under ±10% input/output voltage variation: (a) bipolar grid and (b) unipolar grid. The voltage ratio is 0.5, and DC CMV is injected to enhance the HF CM current reduction.

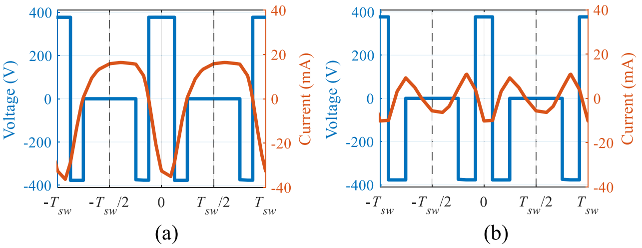

(a) (b)

Fig. 14. Simulated waveforms of CM components of the TS converter using $\boldsymbol{M}_1$ at a voltage ratio of 0.5. (a) Without DC CMV injection. (b) With DC CMV injection ($\boldsymbol{V}_{\mathbf{cm},0} = \; -0.0833\, \boldsymbol{V_{pn}}$) for improved leakage current reduction.

as

$$\sin\left(\pi\left(1-d_{\mathrm{dm}}\right)\right)=2\sin\left(\pi\frac{1-d_{\mathrm{dm}}-2\left|d_{\mathrm{cm}}\right|}{2}\right). \qquad (14)$$

An additional dc CMV is injected into the converter to further reduce the HF leakage current at the nominal operating point by shifting the operating point as close as possible to the minimum-current trajectory. The allowable range of $V_{\mathrm{cm},0}$ is constrained by (9) and (11) for bipolar and unipolar dc grids, respectively. For example, when the converter operates at a voltage ratio of 0.5 under ±10% variation in both input and output voltages $V_{\mathrm{cm},0}$ is limited to the range $[-0.175\, V_{pn}, 0.175\, V_{pn}]$ in the bipolar grid and $[-0.225\, V_{pn}, 0.125\, V_{pn}]$ in the unipolar grid. The value of $V_{\mathrm{cm},0}$ that eliminates the fundamental component of CMV, as derived from (14), is $\pm 0.0833\, V_{pn}$. Since this value lies within the operable range in both bipolar and unipolar grid configurations, dc CMV injection is feasible in both cases. The resulting shift in the operable range along the d_{cm} axis due to the injected $V_{\mathrm{cm},0}$ is illustrated in Fig. 13. The effect of dc CMV injection is shown in Fig. 14(b), where the modified CMV waveform leads to a noticeable reduction in leakage current. By eliminating the fundamental component of CMV, the rms leakage current is significantly reduced.

C. Switching Loss Characteristics of TS Converter

In comparison to the conventional HB converter, the TS converter using hybrid modulation does not exhibit a linear increase in switching loss, despite the fact that the number of switches is doubled. This phenomenon is explained through a comparison of the switching transition events between the two converters. To illustrate this point, consider the switching process of M_3 in Fig. 11(c). The TS converter undergoes four switching transition sequences, specifically U_2–U_3–U_1–U_3–U_2. WhenS_L is shorted without switching, the converter effectively reduces to a two-switch structure composed of S_H and S_M, which is equivalent to the conventional HB converter. Thus, the switching transition of the HB converter corresponds to the same transition sequence U_2–U_3–U_2 in the TS converter. In this case, the current flowing through the HB formed by S_H and S_M equals the output current of the bridge, which corresponds to the sum of DM and CM currents. Meanwhile, the additional transitionU_1 and U_3 in the TS converter, inserted for LF CMV control, switches S_H and S_L while keeping S_M shorted. Here, the current flowing through the equivalent HB composed of S_H and S_L corresponds to the CM current flowing through the converter. Since the magnitude of the CM current, reduced by the CM filter, is smaller than the DM current, the losses in the switching transition between U_1 and U_3 are small compared with those between U_3 and U_2. A similar analogy applies to the M_1 sequence in Fig. 11(a), but in reverse. Therefore, the TS converter with hybrid modulation is an effective method for reducing the LF and HF CM currents without significantly increasing the switching losses compared with the conventional HB converter.

V. SIMULATION AND EXPERIMENTAL RESULTS

In this section, a comparative analysis between the TS converter and other HB-based converters is conducted through simulation. Proposed leakage current suppression strategies of the TS converter are then experiment-ally validated using a hardware prototype, as shown in Fig. 15(a). System parameters are specified in Table V. The converter operates at a

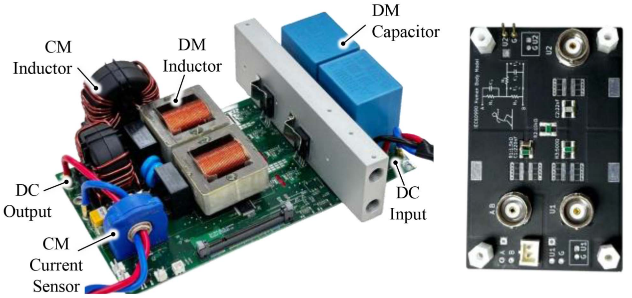

(a) (b)

Fig. 15. Hardware prototypes. (a) 11 kW nonisolated TS converter. (b) Human body impedance model used for touch current measurement.

TABLE V
HARDWARE SPECIFICATIONS

Symbol	Value	Symbol	Value
V_{pn}	750 V	V_{qr}	525 V
f_{sw}	40 kHz	$L_{dm,1}$	220 μH
$L_{cm,1}$	0.5 mH	$L_{cm,2}$	1.0 mH
C_{dc}	110 μF	$C_{dm,1}$	25.6 μF
C_y	470 nF	$C_{cm,1}$	1.36 μF

switching frequency of 40 kHz, with a rated power of 11 kW, achieving a power density of 3.15 kW/dm^3 within a volume of $245 \times 190 \times 75$ mm^3. In the TN grounding system, the chassis is connected to the grid neutral and is disconnected in the event of a ground fault. For touch current measurements, a human body impedance model is implemented using the equivalent circuit shown in Fig. 15(b). The prototype utilizes 1200 V SiC MOSFETS (Infineon IMZC120R012M2H).

Despite the extensive research conducted on LVdc grid voltage selection [1], [3], there still exists no precise regulatory framework for LVdc voltage selection [57]. In this study, based on 1500 V and 750 V utilized in traction systems, 750 V and ±375 V are employed, depending on the grid polarity [1], [58]. In addition, with regard to the voltage maintenance regulations of the ac grid, the range of voltage fluctuations that can occur in the grid under normal circumstances is assumed to be ±10% [59]. The actual dc grid is simulated to reflect the voltage fluctuations that may occur during normal operation. The specific experimental conditions and the analysis of the results are described in the following sections. The voltage fluctuation slope is set to 30 V/ms, which is representative of typical grid-induced disturbances [40], [41].

A. Simulation Results

A comparative analysis is conducted through simulations, evaluating the performance of different HB-based nonisolated dc–dc converter topologies in suppressing CM current. The conventional HB, FB, stacked HB, and TS converter are employed. System parameters are specified in Table V. The nominal voltage of the bipolar grid is ±375 V, and the output voltage is 525 V at an output power of 11 kW. The TN grounding system is applied. Voltage fluctuations of the negative input voltage are introduced, involving a 10% variation from its nominal value. The voltage fluctuation slope is set to 30 V/ms. The leakage current and the neutral line current of the converter topologies are shown in Fig. 16.

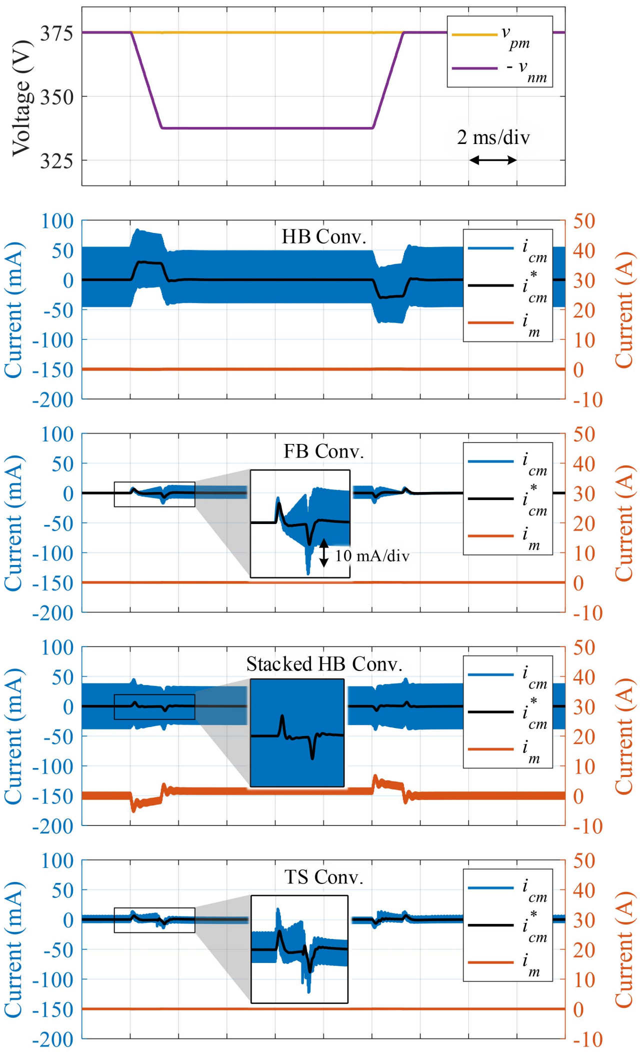

Fig. 16. Simulated waveforms of the HB-based nonisolated DC–DC converter topology. Leakage current and neutral line current for each topology in the presence of a 10% variation of the negative pole in a bipolar grid with an input nominal voltage of ±375 V are shown.

Since the HB converter does not require neutral line current from the input capacitor, the neutral line current is zero. However, conventional HB converters are incapable of reducing LF leakage current under voltage fluctuations of the grid. The leakage current reaches up to 83.9 mA, with a rms of 32.5 mA.

In contrast, the FB converter is capable of injecting CMV to suppress LF leakage current. As it does not require the neutral line current of the input capacitor, the neutral line current is zero. The CM current is suppressed by the leakage current controller proposed in Section III and the modulation method that suppresses the HF CM current [41]. The leakage current reaches up to 17.3 mA, with a rms of 7.25 mA. The overshoot of the LF CM current during voltage fluctuations is 6.5 mA, and the settling time is 0.46 ms.

The stacked HB converter is capable of injecting CMV as well. However, the neutral line current is necessary to balance the input capacitor voltage during CMV injection or voltage fluctuation. The mean value of the neutral line current is 1.55 A, with a maximum of 12.1 A during leakage current suppression. This causes additional conduction losses through the neutral line and increases grid system complexity [5]. The leakage current reaches up to 45.0 mA, with a rms of 23.9 mA, when the CM current controller proposed in Section III and the modulation method in [35] and [36] are employed. The overshoot of the LF CM current during voltage fluctuations is 6.8 mA, and the settling time is 0.63 ms.

The TS converter does not require a neutral line current. The leakage current reaches up to 14.3 mA, with a rms of 2.40 mA, when the CM current controller proposed in Section III and the hybrid modulation method proposed in Section IV are employed. In comparison to the conventional HB, FB, and stacked HB converters, the proposed modulation method with the TS converter exhibits a substantial reduction in HF leakage current with LF CMV injection. The overshoot of the LF CM current during voltage fluctuations is 6.3 mA, and the settling time is 0.44 ms. The FB, Stacked HB, and TS converter employ the same LF CM modeling and utilize the same CM current controller. Consequently, the transient response of their LF CM suppression performance is similar. With CMV injection, the TS converter achieves the smallest HF CM current.

The simulation results indicate that the TS converter exhibits the same suppression performance for LF leakage current in a bipolar grid as the FB and stacked HB converters. In addition, the TS converter effectively suppresses HF leakage current by employing the proposed hybrid modulation method. Moreover, it requires fewer switches than the FB and stacked HB converter, and unlike the stacked HB converter, it does not necessitate a neutral point current for LF CMV injection. Consequently, it is capable of mitigating LF leakage current when connected to a unipolar grid. Based on these results, the experimental study focuses on comparing the leakage current mitigation performance of the conventional HB and the TS converter.

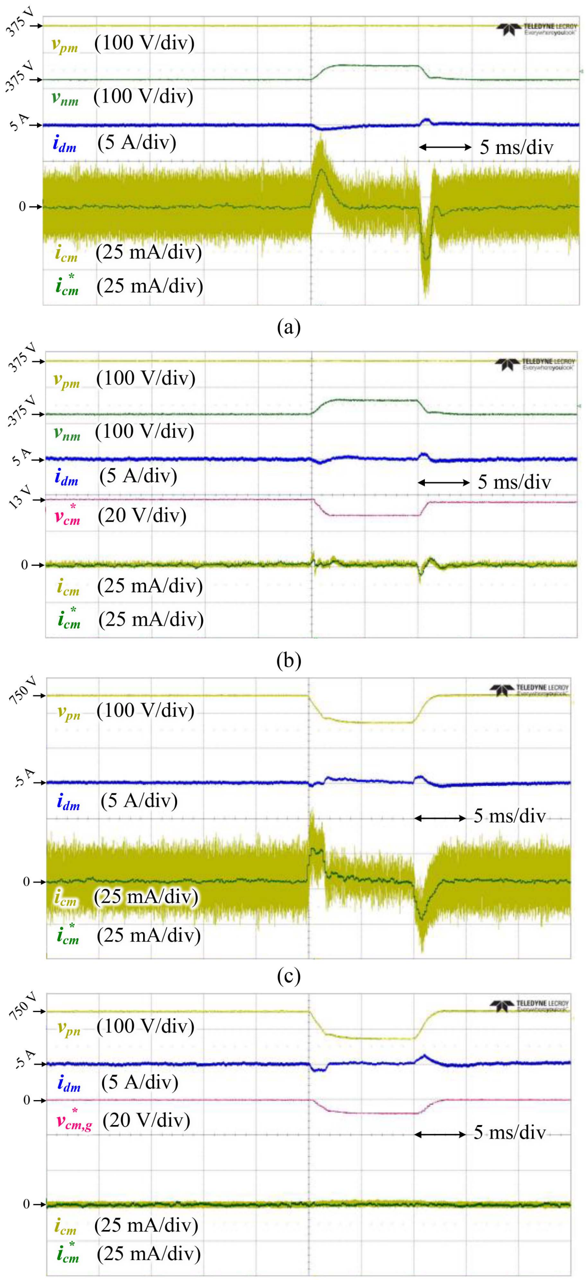

(a)

(b)

(c)

(d)

Fig. 17. Experimental waveforms of nonisolated converters with TN grounding under input voltage fluctuation. (a) HB in a bipolar grid. (b) TS in a unipolar grid. (c) HB in a unipolar grid. (d) TS in a unipolar grid.

B. Leakage Current Suppression

In a bipolar dc grid, the experimental waveform of the conventional HB converter is shown in Fig. 17(a), while Fig. 17(b) presents the waveform of the TS converter. The nominal input voltage is ±375 V, and the output voltage is 525 V. The output DM current is controlled at 5 A. The TN grounding system is applied, and PE is connected to the system neutral line. Fluctuations in the negative input voltage are introduced, involving a 10% variation from its nominal value. As shown in Fig. 17(a), the HB converter successfully regulates the output DM current but fails to suppress leakage current under input voltage disturbances. The voltage fluctuation slope is set to 30 V/ms. The CM current magnitude reaches a peak of 62 mA and a rms of 15.1 mA at the nominal operating point. In contrast, as shown in Fig. 17(b), the TS converter mitigates LF leakage current during the transient through the proposed leakage current controller. Furthermore, the proposed hybrid modulation method effectively reduces the HF CM current, achieving a peak CM current of 13.9 mA and a rms of 1.16 mA at the nominal operation point.

In a unipolar dc grid, the experimental waveforms of the conventional HB converter and the TS converter are shown in Fig. 17(c) and (d), respectively. The nominal input and output voltages are 750 V and 525 V, and the output current is controlled at −5 A. The same TN grounding system is applied. During the test, input voltage and grid CMV fluctuations of 10% and 5% are introduced. As shown in Fig. 17(c), the HB converter fails to suppress leakage current under grid disturbances, with the CM current reaching a peak of 53 mA and a rms of 15.6 mA. In contrast, the TS converter with the proposed hybrid modulation method effectively mitigates both LF and HF CM currents, achieving a peak value of 5.7 mA and a rms of 2.33 mA, as shown in Fig. 17(d).

These experimental results confirm the effectiveness of the proposed leakage current controller and modulation method in suppressing CM currents in both bipolar and unipolar dc grid conditions, while maintaining consistent DM current regulation.

C. Touch Current Suppression

When the grounding wire is disconnected, the CM current no longer bypasses through the ground line; instead, it flows through the human body, posing a serious safety concern. The human body impedance model measures this current, as shown in Fig. 15(b), according to IEC standards [52]. The experimental waveforms of the conventional HB converter and TS converters under grounding loss conditions in both bipolar and unipolar dc grids are represented in Fig. 18. For both cases, the input voltage fluctuation condition remains identical to that of the TN grounding scenario.

In the bipolar configuration, the conventional HB converter, as shown in Fig. 18(a), fails to suppress the touch current (i_{tc}) during input voltage transients, resulting in a peak value of 12.1 mA, which exceeds the safety regulation limit. In contrast, the TS converter in Fig. 18(b) significantly reduces the transient touch current through LF CM component sensing and control, limiting the peak current to 1.4 mA and thereby satisfying the safety requirement.

Similarly, in the unipolar configuration, the conventional HB converter, as shown in Fig. 18(c), produces a peak touch current of 10.5 mA, again exceeding the safety regulation limit. As shown in Fig. 18(d), the TS converter effectively mitigates the touch current, limiting the peak value to 0.34 mA.

These results confirm that the proposed leakage current controller ensures user safety by reducing the touch current within permissible limits, even in the absence of a grounding connection.

D. Modulation

The experimental waveforms of the TS converter with different modulation methods are presented in Fig. 19. The input voltage is 750 V, the output voltage is 525 V, and the DM duty ratio is 0.7. The output current is controlled at 5 A. Fig. 19(a) shows the CM voltage and current waveforms of the conventional HB converter. In contrast, Fig. 19(b), (d), and (e) illustrates those of the TS converter employing modulation M_1, M_2, and M_3, respectively. Overall, the TS converter achieves significantly lower HF CM current than the HB converter, particularly when modulation M_1 or M_3 is applied. Among the three modulation methods of the TS converter, M_2 generates the highest HF CM current due to a significant fundamental component in the CM voltage. In contrast, M_1 and M_3 yield significantly lower HF CM currents. In the proposed hybrid modulation scheme, M_1 and M_3 are alternately applied based on the sign of the CMV.

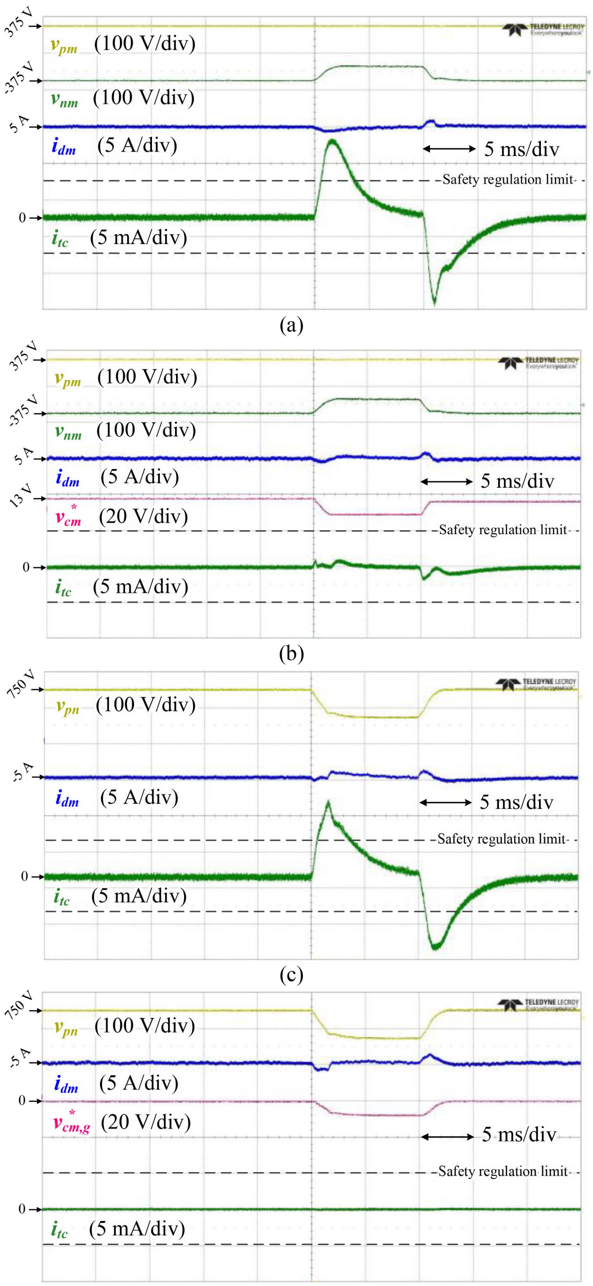

(a)

(b)

(c)

(d)

Fig. 18. Experimental waveforms of nonisolated converters under a loss of grounding condition. (a) HB in a bipolar grid. (b) TS in a unipolar grid. (c) HB in a unipolar grid. (d) TS in a unipolar grid.

To further suppress the HF CM current, an additional dc CMV of –13.1 V is injected for M_1 and 13.1 V for M_3, as shown in Fig. 19(c) and (f). These values are derived from (14) to ensure that the fundamental component of the CM voltage becomes zero, thereby aligning the operating point P with the condition for minimum HF CM current. Fig. 20 summarizes the rms values of the HF CM current for each case. In the HB converter, the rms value is 15.5 mA. For the TS converter, the values are 1.47 mA (M_1), 18.4 mA (M_2), and 1.96 mA (M_3). With dc

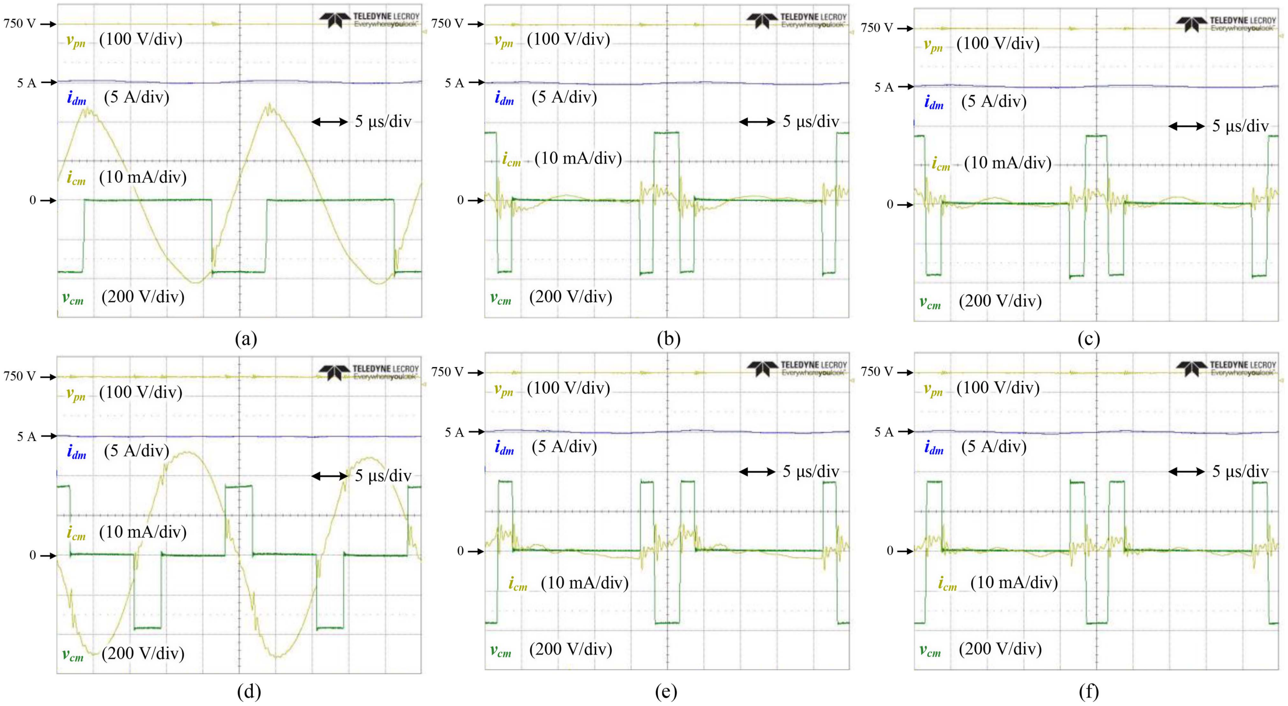

(a) (b) (c)

(d) (e) (f)

Fig. 19. Experimental results of high-frequency CMV and leakage current with different topologies and modulation methods in a TN grounding system. (a) Half-bridge. (b) TS with M_1 (no DC CMV injection). (c) M_1 (with DC CMV injection). (d) M_2. (e) M_3 (no DC CMV injection). (f) M_3 (with DC CMV injection).

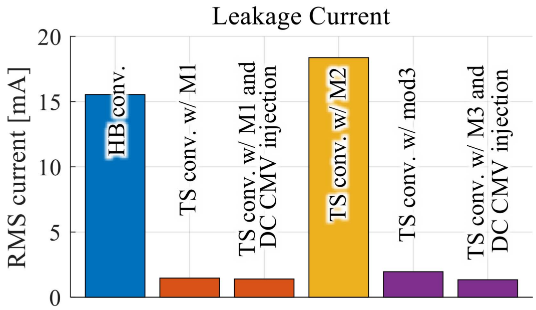

Fig. 20. Measured touch current with various topologies and modulation methods in a TN grounding system.

CMV injection, the current is further reduced to 1.40 mA for M_1 and 1.34 mA for M_3.

These experimental results validate that the proposed modulation method effectively reduces the HF CM current and that the additional dc CMV injection further enhances the suppression performance.

E. Efficiency

The efficiency of the converter, measured up to a rated power of 11 kW, is illustrated in Fig. 21 for input–output voltage ratios of 0.7 and 0.9. Measurements were obtained using a Voltech PM6000 power meter. The conventional HB converter achieves a maximum efficiency of 99.45% at a duty ratio of 0.9 and 98.87% at a duty ratio of 0.7. The TS converter reaches 99.38% and 98.83% in the same respective conditions. The loss breakdown of the conventional HB converter and the TS converter at a duty ratio of 0.9 and an output power of 11 kW is presented for comparison, as illustrated in Fig. 22. In contrast to the

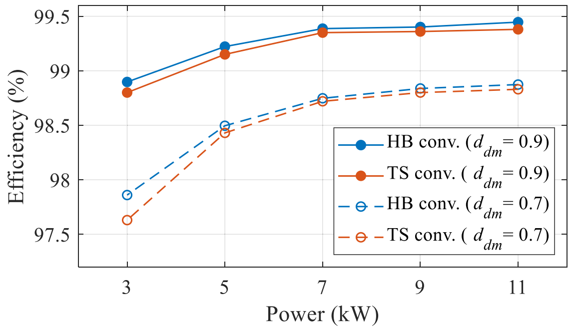

Fig. 21. Measured efficiencies of the 11 kW hardware for the HB and TS converters in varying DM duty ratios and power levels, with a fixed input voltage of 750 V and an identical EMI filter.

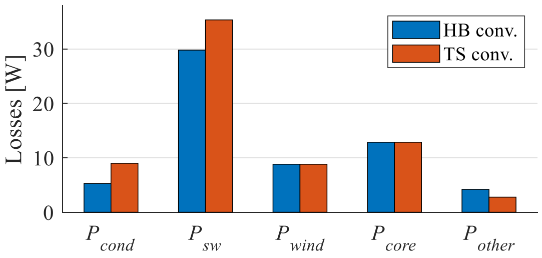

Fig. 22. Loss breakdown of conventional half-bridge converter and TS converter at a voltage ratio of 0.9 and output power 11 kW.

conventional HB converter, the conduction and switching losses of the TS converter increase. As described in Section IV, the switching loss does not increase linearly despite the doubling of the number of switching transitions in the TS converter, resulting in slightly reduced efficiency compared to the conventional HB converter. The core and winding losses are calculated based solely on DM components. Although CM-induced losses contribute additional effects, their accurate quantification requires detailed modeling of localized flux distributions and choke-specific design data, which are beyond the scope of this study. Accordingly, these effects are included in P_{other}, and their impact is expected to be minor compared to DM-dominated losses. In this study, an identical EMI filter is applied to both topologies for a valid comparison. In practical applications, however, the conventional HB converter typically requires a tighter EMI filter to satisfy the same EMI standards, which reduces efficiency and increases system volume. Most importantly, the adoption of the TS topology is intended to suppress LF CM current, thereby enhancing grid compatibility and ensuring human safety.

VI. CONCLUSION

The elimination of galvanic isolation in nonisolated converters presents significant challenges related to CM current generation. To address these issues, this study proposes a comprehensive approach that employs the TS converter topology along with an LF CM current controller, a PWM strategy, and dc CMV injection to reduce HF CM currents.

The key contributions of this study are summarized as follows.

1) HB-based topologies capable of LF CMV injection are compared, and the switching transition characteristics of the TS topology are analyzed.
2) LF CM equivalent circuits are derived based on the dc grid grounding system and polarity configuration. A feedforward-based active CMV control scheme is proposed to suppress the LF CM current.
3) The operable range of the converter is analytically derived to identify the conditions in which both DM current regulation and LF CM current suppression are simultaneously achieved under grid-induced CMV disturbances.
4) A carrier-based PWM method is proposed to reduce the HF CM current. In addition, a dc CMV injection technique is introduced to enhance CM current suppression.

The effectiveness of the proposed methods is validated through experiments using a hardware prototype. Both rms and HF CM currents are significantly reduced, which demonstrates the capability of the proposed approach to mitigate leakage current. The measured touch current is suppressed below the safety threshold, even in the event of a grounding disconnection, ensuring user safety. The converter achieves a peak efficiency of 99.38% at a rated power of 11 kW, highlighting the system's high performance.

In summary, the TS converter, combined with the proposed CM current suppression strategies, offers a practical and reliable solution for transformerless dc–dc power conversion in low-voltage dc grid applications. These contributions ensure both safety and high efficiency, supporting the practical deployment of high-performance nonisolated converters in future dc grid infrastructures.

REFERENCES

[1] E. Rodriguez-Diaz, F. Chen, J. C. Vasquez, J. M. Guerrero, R. Burgos, and D. Boroyevich, "Voltage-level selection of future two-level LVdc distribution grids: A compromise between grid compatibility, safety, and efficiency," *IEEE Electrific. Mag.*, vol. 4, no. 2, pp. 20–28, Jun. 2016.
[2] D. Salomonsson, L. Soder, and A. Sannino, "Protection of low-voltage DC microgrids," *IEEE Trans. Power Del.*, vol. 24, no. 3, pp. 1045–1053, Jul. 2009.
[3] L. Li, K.-J. Li, K. Sun, Z. Liu, and W.-J. Lee, "A comparative study on voltage level standard for DC residential power systems," *IEEE Trans. Ind. Appl.*, vol. 58, no. 2, pp. 1446–1455, Mar./Apr. 2022.
[4] T. Dragičević, X. Lu, J. C. Vasquez, and J. M. Guerrero, "DC microgrids—Part II: A review of power architectures, applications, and standardization issues," *IEEE Trans. Power Electron.*, vol. 31, no. 5, pp. 3528–3549, May 2016.
[5] S. Rivera, R. Lizana F., S. Kouro, T. Dragicevic, and B. Wu, "Bipolar DC power conversion: State-of-the-art and emerging technologies," *IEEE J. Emerg. Sel. Topics Power Electron.*, vol. 9, no. 2, pp. 1192–1204, Apr. 2021.
[6] D. Boroyevich, I. Cvetkovic, R. Burgos, and D. Dong, "Intergrid: A future electronic energy network?," *IEEE J. Emerg. Sel. Topics Power Electron.*, vol. 1, no. 3, pp. 127–138, Sep. 2013.
[7] D. Salomonsson and A. Sannino, "Low-voltage DC distribution system for commercial power systems with sensitive electronic loads," *IEEE Trans. Power Del.*, vol. 22, no. 3, pp. 1620–1627, Jul. 2007.
[8] *Low-voltage electrical installations - Part 1: Fundamental principles, assessment of general characteristics, definitions*, IEC Standard 60364-1, Geneva, Switzerland, 2005.
[9] *Low-voltage electrical installations - Part 4-41: Protection for safety - Protection against electric shock*, IEC Standard 60364-4-41, Geneva, Switzerland, 2005.
[10] J. Mohammadi, F. Badrkhani Ajaei, and G. Stevens, "Grounding the DC microgrid," *IEEE Trans. Ind. Appl.*, vol. 55, no. 5, pp. 4490–4499, Sep./Oct. 2019.
[11] M. Azizi, O. Husev, O. Veligorskyi, S. Rahimpour, and C. Roncero-Clemente, "Grounding and isolation requirements in DC microgrids: Overview and critical analysis," *Energies*, vol. 16, no. 23, Nov. 2023, Art. no. 7747.
[12] S. Beheshtaein, R. M. Cuzner, M. Forouzesh, M. Savaghebi, and J. M. Guerrero, "DC microgrid protection: A comprehensive review," *IEEE J. Emerg. Sel. Topics Power Electron.*, Early Access Article, Mar. 12, 2019, doi: 10.1109/JESTPE.2019.2904588.
[13] D. Kumar, F. Zare, and A. Ghosh, "DC microgrid technology: System architectures, AC grid interfaces, grounding schemes, power quality, communication networks, applications, and standardizations aspects," *IEEE Access*, vol. 5, pp. 12230–12256, 2017.
[14] B. Zhao, Q. Song, W. Liu, and Y. Sun, "Overview of dual-active-bridge isolated bidirectional DC–DC converter for high-frequency-link power-conversion system," *IEEE Trans. Power Electron.*, vol. 29, no. 8, pp. 4091–4106, Aug. 2014.
[15] S. A. Gorji, H. G. Sahebi, M. Ektesabi, and A. B. Rad, "Topologies and control schemes of bidirectional DC–DC power converters: An overview," *IEEE Access*, vol. 7, pp. 117997–118019, 2019.
[16] J. Wang et al., "Nonisolated electric vehicle chargers: Their current status and future challenges," *IEEE Electrific. Mag.*, vol. 9, no. 2, pp. 23–33, Jun. 2021.
[17] S. J. Lee, J. Choi, G. C. Lim, S. M. Kim, E.-K. Kim, and J.-I. Ha, "Analysis and mitigation of bearing current in inverter-fed IPMSMs drive system," *IEEE Trans. Ind. Electron.*, vol. 72, no. 4, pp. 3503–3513, Apr. 2025, doi: 10.1109/TIE.2024.3456435.
[18] W. Li, Y. Gu, H. Luo, W. Cui, X. He, and C. Xia, "Topology review and derivation methodology of single-phase transformerless photovoltaic inverters for leakage current suppression," *IEEE Trans. Ind. Electron.*, vol. 62, no. 7, pp. 4537–4551, Jul. 2015.
[19] L. Zhang, K. Sun, Y. Xing, and M. Xing, "H6 transformerless full-bridge PV grid-tied inverters," *IEEE Trans. Power Electron.*, vol. 29, no. 3, pp. 1229–1238, Mar. 2014.

[20] L. Zhang, K. Sun, L. Feng, H. Wu, and Y. Xing, "A family of neutral point clamped full-bridge topologies for transformerless photovoltaic grid-tied inverters," *IEEE Trans. Power Electron.*, vol. 28, no. 2, pp. 730–739, Feb. 2013.

[21] B. Ji, J. Wang, and J. Zhao, "High-efficiency single-phase transformerless PV H6 inverter with hybrid modulation method," *IEEE Trans. Ind. Electron.*, vol. 60, no. 5, pp. 2104–2115, May 2013.

[22] D. A. Rendusara and P. N. Enjeti, "An improved inverter output filter configuration reduces common and differential modes dv/dt at the motor terminals in PWM drive systems," *IEEE Trans. Power Electron.*, vol. 13, no. 6, pp. 1135–1143, Nov. 1998.

[23] L. LaWhite and M. F. Schlecht, "Design of active ripple filters for power circuits operating in the 1-10 MHz range," *IEEE Trans. Power Electron.*, vol. 3, no. 3, pp. 310–317, Jul. 1988.

[24] Y.-C. Son and S.-K. Sul, "A new active common-mode EMI filter for PWM inverter," *IEEE Trans. Power Electron.*, vol. 18, no. 6, pp. 1309–1314, Nov. 2003.

[25] J. Biela, A. Wirthmueller, R. Waespe, M. L. Heldwein, K. Raggl, and J. W. Kolar, "Passive and active hybrid integrated EMI filters," *IEEE Trans. Power Electron.*, vol. 24, no. 5, pp. 1340–1349, May 2009.

[26] M. Sagar Bhaskar et al., "Survey of DC-DC non-isolated topologies for unidirectional power flow in fuel cell vehicles," *IEEE Access*, vol. 8, pp. 178130–178166, 2020.

[27] R. Venugopal et al., "Review on unidirectional non-isolated high gain DC–DC converters for EV sustainable DC fast charging applications," *IEEE Access*, vol. 11, pp. 78299–78338, 2023.

[28] J.-W. Shin, H. Shin, G.-S. Seo, J.-I. Ha, and B.-H. Cho, "Low-common mode voltage H-bridge converter with additional switch legs," *IEEE Trans. Power Electron.*, vol. 28, no. 4, pp. 1773–1782, Apr. 2013, doi: 10.1109/TPEL.2012.2213844.

[29] M. Forouzesh, Y. P. Siwakoti, S. A. Gorji, F. Blaabjerg, and B. Lehman, "Step-up DC–DC converters: A comprehensive review of voltage-boosting techniques, topologies, and applications," *IEEE Trans. Power Electron.*, vol. 32, no. 12, pp. 9143–9178, Dec. 2017.

[30] R. W. Erickson and D. Maksimović, "Converter circuits," in *Fundamentals of Power Electronics*, 3rd ed. Berlin, Germany: Springer, 2020, ch. 6, pp. 163–204.

[31] G.-H. Min, H. Kwon, J. Lee, and J.-I. Ha, "Virtually isolated class e converter with coupled capacitors," in *Proc. IEEE Appl. Power Electron. Conf. Expo.*, Orlando, FL, USA, Mar. 2023, pp. 2124–2128, doi: 10.1109/APEC43580.2023.10131604.

[32] J.-S. Hong and J.-I. Ha, "Transformer-less series-input-parallel-output dual active half-bridge for MV-LV DC/DC converter," in *Proc. IEEE Appl. Power Electron. Conf. Expo.*, New Orleans, LA, USA, Mar. 2020, pp. 1061–1066. doi: 10.1109/APEC39645.2020.9124334.

[33] J. Zhu, M. Xu, J. Sun, and C. Wang, "Novel capacitor-isolated power converter," in *Proc. IEEE Energy Convers. Congr. Expo.*, Atlanta, GA, USA, Sep. 2010, pp. 1824–1829.

[34] G. V. den Broeck, W. Martinez, M. Dalla Vecchia, S. Ravyts, and J. Driesen, "Conversion efficiency of the buck three-level DC–DC converter in unbalanced bipolar DC microgrids," *IEEE Trans. Power Electron.*, vol. 35, no. 9, pp. 9306–9319, Sep. 2020.

[35] Y. Cao et al., "A three-level buck–boost converter with planar coupled inductor and common-mode noise suppression," *IEEE Trans. Power Electron.*, vol. 38, no. 9, pp. 10483–10500, Sep. 2023.

[36] L. Tan, B. Wu, S. Rivera, and V. Yaramasu, "Comprehensive DC power balance management in high-power three-level DC–DC converter for electric vehicle fast charging," *IEEE Trans. Power Electron.*, vol. 31, no. 1, pp. 89–100, Jan. 2016.

[37] D. Zhang, D. Cao, J. Huber, J. Everts, and J. W. Kolar, "Nonisolated three-phase current DC-link buck–boost EV charger with virtual output midpoint grounding and ground current control," *IEEE Trans. Transp. Electrific.*, vol. 10, no. 1, pp. 1398–1413, Mar. 2024.

[38] T. R. Oliveira, W. W. A. G. Silva, S. I. Seleme, and P. F. Donoso-Garcia, "PLL-based feed-forward control to attenuate low-frequency common-mode voltages in transformerless LVDC systems," *IEEE Trans. Ind. Appl.*, vol. 55, no. 3, pp. 3151–3159, May/Jun. 2019.

[39] F. Chen, R. Burgos, and D. Boroyevich, "A bidirectional high-efficiency transformerless converter with common-mode decoupling for the interconnection of AC and DC grids," *IEEE Trans. Power Electron.*, vol. 34, no. 2, pp. 1317–1333, Feb. 2019.

[40] D. Dong, F. Luo, D. Boroyevich, and P. Mattavelli, "Leakage current reduction in a single-phase bidirectional AC–DC full-bridge inverter," *IEEE Trans. Power Electron.*, vol. 27, no. 10, pp. 4281–4291, Oct. 2012.

[41] J. Lee, D. Lee, and J.-I. Ha, "Control and modulation methods of single-/three-phase PWM converter for suppressing leakage current," *IEEE Trans. Power Electron.*, vol. 40, no. 7, pp. 9137–9152, Jul. 2025, doi: 10.1109/TPEL.2025.3546298.

[42] D. Lee, J. Lee, and J.-I. Ha, "DC-link voltage reduction with synergetic common-mode voltage control of single-phase two-stage non-isolated EV chargers," in *Proc. IEEE Appl. Power Electron. Conf. Expo.*, Mar. 2025, pp. 457–463, doi: 10.1109/APEC48143.2025.10977561.

[43] *Information technology equipment - Safety - Part 1: General requirements*, IEC Standard 60950-1, Geneva, Switzerland, 2016.

[44] D.-I. Lee, S.-M. Hong, J.-B. Lee, H.-S. Youn, D.-W. Lee, and Y.-S. Lee, "Nonisolated on-board charger capable of reducing common-mode leakage current and balancing voltage of Y-capacitor on high-voltage battery," *IEEE Trans. Transp. Electrific.*, vol. 11, no. 2, pp. 6572–6589, Apr. 2025.

[45] F. A. Kharanaq, A. Emadi, and B. Bilgin, "Modeling of conducted emissions for EMI analysis of power converters: State-of-the-art review," *IEEE Access*, vol. 8, pp. 189313–189325, 2020.

[46] L. Ran, S. Gokani, J. Clare, K. J. Bradley, and C. Christopoulos, "Conducted electromagnetic emissions in induction motor drive systems. I. Time domain analysis and identification of dominant modes," *IEEE Trans. Power Electron.*, vol. 13, no. 4, pp. 757–767, Jul. 1998.

[47] T. Kerekes, R. Teodorescu, M. Liserre, C. Klumpner, and M. Sumner, "Evaluation of three-phase transformerless photovoltaic inverter topologies," *IEEE Trans. Power Electron.*, vol. 24, no. 9, pp. 2202–2211, Sep. 2009.

[48] Y. Gu, W. Li, and X. He, "Analysis and control of bipolar LVDC grid with DC symmetrical component method," *IEEE Trans. Power Syst.*, vol. 31, no. 1, pp. 685–694, Jan. 2016.

[49] T.-H. Chen and W.-C. Yang, "Analysis of multi-grounded four-wire distribution systems considering the neutral grounding," *IEEE Trans. Power Del.*, vol. 16, no. 4, pp. 710–717, Oct. 2001.

[50] T. R. De Oliveira, A. S. Bolzon, and P. F. Donoso-Garcia, "Grounding and safety considerations for residential DC microgrids," in *Proc. 40th Annu. Conf. IEEE Ind. Electron. Soc.*, Dallas, TX, USA, Oct. 2014, pp. 5526–5532.

[51] J.-D. Park and J. Candelaria, "Fault detection and isolation in low-voltage DC-bus microgrid system," *IEEE Trans. Power Del.*, vol. 28, no. 2, pp. 779–787, Apr. 2013.

[52] *Methods of measurement of touch current and protective conductor current*, IEC Standard 60990, Geneva, Switzerland, 2016.

[53] P. Kumar and M. Rojas-Gonzalez, "Novel 3-switch dual output buck voltage regulator," in *Proc. 21st Annu. IEEE Appl. Power Electron. Conf. Expo.*, Mar. 2006, pp. 467–473.

[54] P. Kumar, "Multiple output buck converter," U.S. Patent 7511463, Mar. 31, 2009.

[55] G. Chen, Z. Jin, Y. Liu, Y. Hu, J. Zhang, and X. Qing, "Programmable topology derivation and analysis of integrated three-port DC–DC converters with reduced switches for low-cost applications," *IEEE Trans. Ind. Electron.*, vol. 66, no. 9, pp. 6649–6660, Sep. 2019.

[56] D. Han, W. Lee, S. Li, and B. Sarlioglu, "New method for common mode voltage cancellation in motor drives: Concept, realization, and asymmetry influence," *IEEE Trans. Power Electron.*, vol. 33, no. 2, pp. 1188–1201, Feb. 2018.

[57] *LVDC systems - Assessment of standard voltages and power quality requirements*, IEC TR 63282, 2024.

[58] *Railway applications - Supply voltages of traction systems*, IEC Standard 60850, Geneva, Switzerland, 2014.

[59] *Voltage characteristics of electricity supplied by public electricity networks*, BS EN 50160, London, United Kingdom, 2022.

Dongsu Lee (Student Member, IEEE) was born in Seoul, South Korea, in 1996. He received the B.S. degree in automotive engineering in 2021 from Hanyang University, Seoul, South Korea, where he is currently working toward the Ph.D. degree in electrical engineering.

His research interests include nonisolated electric vehicle chargers, transformerless ac–dc/dc–dc/ac–ac converter, virtual isolation, and grid connected power-factor-correcting ac–dc converter.

Juwon Lee (Student Member, IEEE) was born in Seoul, South Korea, in 1997. He received the B.S. degree in electrical engineering in 2020 from Seoul National University, Seoul, South Korea, where he is currently working toward the Ph.D. degree in electrical engineering.

His current research interests include electric energy conversion, grid-connected converter, and design and control of transformerless ac–dc/dc–dc converter.

Jung-Ik Ha (Fellow, IEEE) received the B.S., M.S., and Ph.D. degrees in electrical engineering from Seoul National University (SNU), Seoul, South Korea, in 1995, 1997, and 2001, respectively.

From 2001 to 2002, he was a Researcher with Yaskawa Electric Company, Japan. From 2003 to 2008, he was with the Samsung Electronics Company, South Korea, as a senior and principal Engineer. From 2009 to 2010, he was a Chief Technology Officer, LS Mecapion Company, South Korea. Since 2010, he has been with the Department of Electrical and Computer Engineering, SNU, where he is currently a Full Professor. From 2016 to 2017, he was a Visiting Scholar with Massachusetts Institute of Technology, Cambridge, MA, USA. He has authored and coauthored more than 300 international journals and conference papers in the area of power electronics and motor drives. His research interests include circuits and control in high efficiency and integrated electric energy conversions for various industrial fields.

Dr. Ha has been an Associate Member with the National Academy of Engineering of Korea since 2023, and the Director with Electric Power Research Institute, SNU, since 2024. He was the Editor-in-Chief of *Journal of Power Electronics* from 2018 to 2021 and a Vice Dean with the College of Engineering, SNU, from 2021 to 2022.